The Temperature Anomaly Pattern of the Pacific–North American Teleconnection: Growth and Decay

JOSEPH P. CLARK[a] AND STEVEN B. FELDSTEIN[a]

[a] *Department of Meteorology and Atmospheric Science, The Pennsylvania State University, University Park, Pennsylvania*

(Manuscript received 3 February 2021, in final form 14 January 2022)

ABSTRACT: Applying composite analysis to ERA-Interim data, the surface air temperature (SAT) anomaly pattern of the Pacific–North American (PNA) teleconnection is shown to include both symmetric and asymmetric SAT anomalies with respect to the PNA phase. The symmetric SAT anomalies, overlying the Russian Far East and western and eastern North America, grow through advection of the climatological temperature by the anomalous meridional wind and vertical mixing. The asymmetric SAT anomalies, overlying Siberia during the positive PNA and the subtropical North Pacific during the negative PNA, grow through vertical mixing only. For all SAT anomalies, vertical mixing relocates the temperature anomalies of the PNA teleconnection pattern from higher in the boundary layer downward to the level of the SAT. Above the level of the SAT, temperature anomaly growth is caused by horizontal temperature advection in all locations except for the subtropical North Pacific, where adiabatic cooling dominates. SAT anomaly decay is caused by longwave radiative heating/cooling, except over Siberia, where SAT anomaly decay is caused by vertical mixing. Additionally, temperature anomaly decay higher in the boundary layer due to nonlocal mixing contributes indirectly to SAT anomaly decay by weakening downgradient diffusion. These results highlight a diverse array of mechanisms by which individual anomalies within the PNA pattern grow and decay. Furthermore, with the exception of Siberia, throughout the growth and decay stages, horizontal temperature advection and/or vertical mixing is nearly balanced by longwave radiative heating/cooling, with the former being slightly stronger during the growth stage and the latter during the decay stage.

KEYWORDS: Dynamics; Planetary waves; Teleconnections

1. Introduction

The Pacific–North American (PNA) teleconnection pattern has long been recognized as a dominant mode of weather and climate variability observed over the Northern Hemisphere (Walker and Bliss 1932; Wallace and Gutzler 1981; Blackmon et al. 1984a,b; Barnston and Livezey 1987; Feldstein 2002). With an intrinsic growth and decay time scale of about 2 weeks (Feldstein 2000, 2002), the PNA impacts not only intraseasonal weather, but it also influences interannual climate (e.g., Blackmon et al. 1984a,b), as a 2-week time scale provides enough memory to generate interannual climate noise (Leith 1973; Madden 1976; Madden and Shea 1978; Feldstein 2000). The mechanisms that drive the growth and decay of the PNA therefore remain an important topic of continuing research.

On the growth of the PNA, many studies agree that tropical convection is an important ingredient (e.g., Horel and Wallace 1981; Mori and Watanabe 2008; Dai et al. 2017), as tropical convection generates poleward-propagating Rossby waves reminiscent of the PNA pattern (e.g., Hoskins and Karoly 1981). However, additional ingredients may also be important for PNA growth. For example, some fraction of PNA events are suggested to arise as subtropical convection generates Rossby waves, without any contribution from convection in the deep tropics (Dai et al. 2017). Furthermore, two other processes have been found to play an important role for PNA growth. After the PNA pattern has been excited by convection, it has been shown that further amplification of the PNA arises through driving by high-frequency transient eddy vorticity fluxes (Feldstein 2002). Morphologically, these high-frequency eddies that amplify the PNA correspond to cyclonic (anticyclonic) breaking of synoptic-scale waves for the positive (negative) phase of the PNA (Franzke et al. 2011). Additionally, both modeling (Simmons et al. 1983; Branstator 1990, 1992) and observational (Feldstein 2002; Mori and Watanabe 2008; Franzke et al. 2011; Dai et al. 2017) studies of the PNA showed that the extraction of kinetic energy from the zonally varying basic state by planetary-scale transient eddies also makes an important contribution to the growth of the PNA. A different perspective was presented by Cash and Lee (2001), who showed that 68% (70%) of the positive (negative) PNA events arise from optimal growth, which suggests that the majority of PNA events, for both phases, arise from the constructive interference of decaying modes. The above processes present hypotheses for generating the upper-tropospheric circulation anomalies associated with the PNA. As was shown in Black and Dole (1993), by performing potential vorticity inversions, the PNA's upper-tropospheric circulation anomalies can induce circulation anomalies that reach downward all the way to the surface.

Although PNA decay has perhaps received less attention than PNA growth, many studies conclude that low-frequency eddy vorticity fluxes in the upper troposphere play an important role in PNA decay (e.g., Dai et al. 2017; Mori and

Supplemental information related to this paper is available at the Journals Online website: https://doi.org/10.1175/JAS-D-21-0030.s1.

Corresponding author: Joseph P. Clark, juc414@psu.edu

DOI: 10.1175/JAS-D-21-0030.1

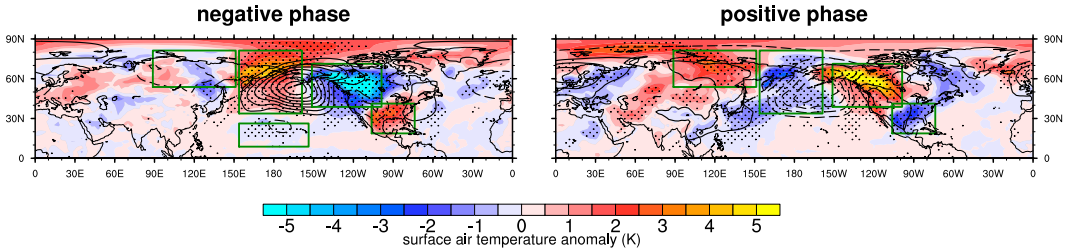

FIG. 1. Surface (2-m) temperature anomaly composite for the (left) negative and (right) positive PNA phases. The corresponding sea level pressure anomaly composites are overlaid in the contours. Dashed contours denote negative sea level pressure anomaly values and solid contours denote positive sea level pressure anomaly values. The zero contour is omitted and the contour interval is 2.5 hPa.

Watanabe 2008). Feldstein (2002) also notes that the PNA decay may be caused by frictional processes via Ekman pumping in the atmosphere, which can weaken upper-tropospheric streamfunction anomalies by inducing rising motion and upper-tropospheric horizontal divergence where there are anomalous cyclones and vice versa.

Apart from the drivers of PNA growth and decay, an interesting and distinguishing feature of the PNA is its asymmetry with respect to the phase (e.g., Mori and Watanabe 2008; Franzke et al. 2011). In particular, the positive PNA is associated with an upstream Eurasian wave train in the upper troposphere that is usually absent for the negative PNA (Mori and Watanabe 2008; Franzke et al. 2011). This appears to be true at least for PNA events associated with tropical convection (Dai et al. 2017).

While many aspects of PNA growth and decay remain a subject of continuing research, the motivation is consistent: the PNA has significant impacts on the weather and climate over the North American continent and across the Northern Hemisphere (e.g., Namias 1969; Dickson and Namias 1976; Leathers et al. 1991; Notaro et al. 2006; Harding and Snyder 2015). These impacts include, but are not limited to, changes in precipitation (e.g., Leathers et al. 1991; Harding and Snyder 2015), storm frequency (e.g., Dickson and Namias 1976), lake-effect snowfall (Notaro et al. 2006), the jet stream (Harding and Snyder 2015), and the surface air temperature (SAT) (e.g., Leathers et al. 1991). In this paper, we focus on the SAT anomaly pattern of the PNA, which is composed of SAT anomalies across not only over North America, but over the Northern Hemisphere in general (Fig. 1).

Despite their importance, the drivers of the PNA's SAT anomalies remain little explored. This is perhaps due to a common assumption that SAT anomalies produced on intraseasonal time scales are caused by horizontal temperature advection (e.g., Namias 1978; Leathers et al. 1991; Yu and Lin 2019). However, this cannot be known with full confidence without a detailed analysis in which each term in the thermodynamic energy equation is evaluated at the level of the SAT. In addition, the mechanisms that drive the PNA's SAT anomaly decay have scarcely been considered. The primary purpose of this study is therefore to investigate what processes drive the growth and decay of each SAT anomaly associated with both PNA phases. We begin with a discussion of the data and methods used (section 2). Next, in section 3, we present results including a discussion of phase asymmetries and budget analyses. Finally, we conclude in section 4 with a summary of the main findings and their implications for our overall understanding of the PNA.

2. Data and methods

a. The composite method

Before examining the SAT anomalies associated with the PNA during December–February (DJF), we first identify days when the PNA is active, referred to as PNA events. In total, we identify 86 positive PNA events and 79 negative PNA events between 1979 and 2018, where events are defined using the daily PNA index provided by the NOAA/Climate Prediction Center (https://www.cpc.ncep.noaa.gov/products/precip/CWlink/pna/pna.shtml). PNA events are defined to be days when the PNA index 1) deviates from its DJF mean value by more than one standard deviation and 2) attains a peak value (i.e., the derivative changes sign), together with the constraint that the peak PNA index values that satisfy 1 and 2 are separated by more than 12 days. This constraint ensures statistical independence between PNA events as the PNA index has an autocorrelation decay time scale of about 8 days (e.g., Feldstein 2000). For this study, we use European Centre for Medium-Range Weather Forecasts (ECMWF) interim reanalysis (ERA-Interim; Dee et al. 2011) data. Composites are constructed by averaging reanalysis fields for these days and statistical significance is tested by generating a null distribution formed by 250 randomly generated composites with the same number of events. Composites are calculated at time lags extending from lag day −10 to lag day +10, where lag day 0 denotes the day when the PNA index attains its peak amplitude.

b. The thermodynamic energy equations

To diagnose the processes that drive the growth and decay of the PNA's SAT anomalies (the composite SAT anomalies are shown in Fig. 1, whose locations depend on the PNA phase), we examine each term in the thermodynamic energy equation that is utilized in the ECMWF reanalysis model (in hybrid sigma–pressure coordinates, η coordinates):

$$\frac{\partial T}{\partial t} = -u\frac{\partial T}{\partial x} - v\frac{\partial T}{\partial y} - \dot{\eta}\frac{\partial T}{\partial \eta} + \frac{\kappa T\omega}{p} + Q_1 + Q_2 + Q_3 + Q_4, \tag{1}$$

where horizontal diffusion has not been included (see below). The zonal wind u, meridional wind v, vertical velocity ω, temperature T, and diabatic heating terms (Q_1, Q_2, Q_3, and Q_4) are downloaded from the ECMWF reanalysis. The four diabatic heating terms, Q_1, Q_2, Q_3, and Q_4 in (1), respectively correspond to longwave radiative heating/cooling, shortwave radiative heating/cooling, latent heat release, and vertical mixing. The diabatic terms, Q_1, Q_2 and the sum of all diabatic terms ($Q_{\text{tot}} = Q_1 + Q_2 + Q_3 + Q_4$) are downloaded as 12-h accumulations initiated at 0000 and 1200 UTC. We subsequently summed the 12-h accumulations to get the daily mean values of each diabatic term. We determine ($Q_3 + Q_4$) from a residual, i.e., ($Q_3 + Q_4$) = $Q_{\text{tot}} - (Q_1 + Q_2)$. Because ERA-Interim provides vertical mixing and latent heat release as a sum, not allowing Q_3 and Q_4 to be separated, the sum ($Q_3 + Q_4$) is assumed to be dominated by vertical mixing near the surface. Therefore, we refer to the sum of Q_3 and Q_4 as vertical mixing.

All variables are obtained on the lowest η surface, which is a terrain following surface approximately 10 m above the ground (Berrisford et al. 2009). We use data on the lowest η surface for two reasons. First, this surface is the lowest level at which all variables in Eq. (1) are available for download. Second, due to its close proximity with the surface, the temperature anomalies on this level are nearly identical to those at 2 m (not shown). Therefore, it can be reasonably assumed that the processes driving temperature anomalies on the lowest η surface are the same as those that drive the temperature anomalies at 2 m (which is the standard height for the SAT, i.e., the 2-m temperature).

Vertical mixing, Q_4 in Eq. (1), refers to turbulent sensible heat flux convergence (ECMWF 2019; see their chapter 3 for details). In particular, vertical mixing arises from a combination of two processes: local mixing represented by small-scale downgradient K diffusion and nonlocal mixing associated with boundary layer–scale unstable vertical motions represented primarily by strong updraft mass fluxes (ECMWF 2019). The downgradient K diffusion is always used, whether or not the boundary layer is stable or unstable, and the nonlocal mixing is activated only when the boundary layer is unstable. The stability of the boundary layer is determined by the stability of the surface layer, being unstable (stable) for an upward (a downward) surface buoyancy flux (ECMWF 2019).

In our budget analyses, we calculate each term in Eq. (1) and subtract the seasonality from each term, leading to the following equation, where primes signify anomalies,

$$\frac{\partial T'}{\partial t} = -\left[u\frac{\partial T}{\partial x}\right]' - \left[v\frac{\partial T}{\partial y}\right]' - \left[\dot{\eta}\frac{\partial T}{\partial \eta}\right]' + \left[\frac{\kappa T\omega}{p}\right]' + Q_1' + Q_2' + Q_3' + Q_4', \tag{2}$$

which states that temperature anomalies T' on the lowest η surface are driven by a combination of anomalous horizontal temperature advection, $-[u\partial T/\partial x]' - [v\partial T/\partial y]'$, anomalous vertical temperature advection $-[\dot{\eta}\partial T/\partial \eta]'$, anomalous adiabatic warming/cooling $[\kappa T\omega/p]'$, and the anomalous diabatic heating terms, Q_1', Q_2', Q_3', and Q_4'. (Primes superscripting bracketed terms act on the product within the bracket. Brackets have no meaning other than grouping terms.) Following Clark and Feldstein (2020a), anomalies in this study are defined as the deviation from the calendar day mean seasonal cycle, which is smoothed with a Fourier analysis truncated at the tenth harmonic. As stated earlier, the diabatic heating terms are obtained as accumulated daily averages by summing the 0000 and 1200 UTC 12-h accumulations. (Note that the vertical mixing term is not truly diabatic, but as it is parameterized, we consider it as such.) These accumulated averages are computed by the reanalysis model using all model time steps (i.e., a daily average of data with approximately 12-min temporal resolution; ECMWF 2014). This is in contrast with the first four terms on the right-hand side of Eq. (2) which are calculated at a 6-hourly resolution before computing the daily average. For the temperature advection terms, horizontal derivatives are calculated using spherical harmonics. Details about the calculation of the vertical advection term can be found in the appendix section of Clark and Feldstein (2020a). All variables have a horizontal resolution of 2.5° in both latitude and longitude.

It is important to note that Eq. (1) excludes some terms that are included in the ECMWF reanalysis model (ECMWF 2014). In particular, Eq. (1) is missing two important processes. These are horizontal diffusion, which is not available from the ERA-Interim archive, and the analysis step, i.e., temperature changes caused by 12-hourly data assimilation. Therefore, considering the differences in temporal resolution between the dynamical and diabatic heating terms, and the fact that Eq. (1) is missing some processes that occur in the reanalysis model, a budget using Eq. (2) is not expected to be perfectly balanced. In spite of this, however, the budget will still prove to be useful for identifying the dominant processes that underlie the growth and decay of the PNA's SAT anomalies.

To determine what causes changes in horizontal temperature advection, $-\mathbf{u}\cdot\nabla T$, where $\mathbf{u} = (u, v, 0)$ and $\nabla = (\partial/\partial x, \partial/\partial y, 0)$, we let $\mathbf{u} = \overline{\mathbf{u}} + \mathbf{u}'$ and $T = \overline{T} + T'$, and decompose the contributions from the anomalous wind and anomalous temperature as follows:

$$\begin{aligned} -\mathbf{u}\cdot\nabla T + \overline{\mathbf{u}\cdot\nabla T} = &\left(-\mathbf{u}'\cdot\nabla\overline{T} + \overline{\mathbf{u}'\cdot\nabla\overline{T}}\right) + \left(-\overline{\mathbf{u}}\cdot\nabla T' + \overline{\overline{\mathbf{u}}\cdot\nabla T'}\right) \\ &+ \left(-\mathbf{u}'\cdot\nabla T' + \overline{\mathbf{u}'\cdot\nabla T'}\right) \\ &+ \left(-\overline{\mathbf{u}}\cdot\nabla\overline{T} + \overline{\overline{\mathbf{u}}\cdot\nabla\overline{T}}\right), \end{aligned} \tag{3}$$

where all overbars denote smoothed seasonal cycles. Due to the smoothing of the seasonal cycle, $\overline{\mathbf{u}'\cdot\nabla\overline{T}}$, $\overline{\overline{\mathbf{u}}\cdot\nabla T'}$, and $\left(-\overline{\mathbf{u}}\cdot\nabla\overline{T} + \overline{\overline{\mathbf{u}}\cdot\nabla\overline{T}}\right)$ are nearly, but not exactly, equal to zero. (Without smoothing, these three terms would be equal to zero.)

Following the calculation of each term in Eqs. (2) and (3) for all days between 1979 and 2018, we compute composites of PNA events based on days when the PNA index satisfies the criteria discussed above. Composites of each term in Eqs. (2) and (3) are calculated and area averaged within the boxes outlining the major anomalies in Fig. 1 (Table 1). Following a

TABLE 1. Domains of the major temperature anomalies.

Region	Domain	Dominant drivers of SAT anomaly growth	Dominant drivers of SAT anomaly decay
Siberia	55°–80°N, 90°–150°E	Q_4' (vertical mixing)	Q_4' (vertical mixing)
Subtropical North Pacific	10°–25°N, 155°E–155°W	Q_4' (vertical mixing)	Q_1' (longwave radiative heating/cooling)
Russian Far East	35°–80°N, 155°E–160°W	$\left(-\mathbf{u}'\cdot\nabla\overline{T}+\overline{\mathbf{u}'\cdot\nabla\overline{T}}\right)+Q_4'$ (vertical mixing)	Q_1' (longwave radiative heating/cooling)
Western North America	40°–70°N, 150°–100°W	$\left(-\mathbf{u}'\cdot\nabla\overline{T}+\overline{\mathbf{u}'\cdot\nabla\overline{T}}\right)+Q_4'$ (vertical mixing)	Q_1' (longwave radiative heating/cooling)
Eastern North America	20°–40°N, 105°–75°W	$\left(-\mathbf{u}'\cdot\nabla\overline{T}+\overline{\mathbf{u}'\cdot\nabla\overline{T}}\right)+Q_4'$ (vertical mixing)	Q_1' (longwave radiative heating/cooling)

method similar to Seo et al. (2016), Clark and Feldstein (2020a,b), and Clark et al. (2021), the composited area-averaged terms in Eqs. (2) and (3) are integrated forward in time with

$$\int_{-10}^{\text{lag}} A(t)dt \approx \sum_{t=-10}^{\text{lag}} A(t)\delta t, \tag{4}$$

where A denotes any term in Eqs. (2) and (3), with units of K day^{-1}, δt = 1 day is the time step, and lag refers to the composite time lag. The integration in Eq. (4), which has units of kelvins, corresponds to the change in the temperature anomaly associated with term A, i.e., $T'(\text{lag}) - T'(-10)$, on the lowest η surface. This 21-day integration period is long enough to capture the growth and decay of the PNA events.

This methodology, which is applied at the lowest η surface, is then repeated in exactly the same manner to diagnose temperature changes throughout the troposphere using the following thermodynamic energy equation in pressure coordinates (e.g., Holton and Hakim 2013):

$$\frac{\partial T'}{\partial t} = -\left[u\frac{\partial T}{\partial x}\right]' - \left[v\frac{\partial T}{\partial y}\right]' + \left[S_p\omega\right]' + Q_1' + Q_2' + Q_3' + Q_4', \tag{5}$$

where primes again denote a deviation from the smoothed seasonal cycle, $S_p \equiv -(T/\theta)(\partial\theta/\partial p)$, where θ denotes potential temperature, and horizontal derivatives are calculated along constant pressure surfaces. The remaining terms in (5) are identical to those in Eq. (2) and the horizontal temperature advection term in Eq. (5) is decomposed using Eq. (3). The first three terms in Eq. (5) are calculated using ECMWF reanalysis data provided at 0000 UTC. As was done on the lowest η surface, the diabatic terms, Q_1, Q_2 and the sum of all diabatic terms ($Q_{\text{tot}} = Q_1 + Q_2 + Q_3 + Q_4$) are downloaded as 12-h accumulations initiated at 0000 and 1200 UTC. These variables are only obtainable in η coordinates. Therefore, we interpolated their values to pressure coordinates.

3. Results

a. Phase asymmetries

Figure 1 shows the SAT anomaly pattern for both the positive and negative phases of the PNA, from which a striking feature is evident: upstream of North America, the location of the PNA's SAT anomalies for the positive phase are very different from those of the negative phase. For the positive phase of the PNA, there is a pronounced positive SAT anomaly over northeast Siberia that is nonexistent for the negative phase of the PNA. In further contrast, for the negative phase of the PNA, a negative SAT anomaly is present over the subtropical North Pacific that is weakly, if at all, present (with the opposite sign) for the positive phase of the PNA.

Figure 2 shows, as a histogram, the number of PNA events (y axis) as a function of Siberian SAT anomaly value (x axis) (where the Siberian SAT anomaly value is calculated as the area average within the box overlying Siberia in Fig. 1 at lag day 0). A considerable preference for positive Siberian SAT anomalies is evident in Fig. 2b, as the majority of the 86 positive PNA events occur when the SAT anomaly over Siberia is greater than 1 K. Specifically, 44 positive PNA events have a Siberian SAT anomaly value of greater than 1.0. Also, 55 positive PNA events have a Siberian SAT anomaly value of greater than 0.0. The mean of the distribution shown in Fig. 2b is 1.52 K, which is statistically significant at p = 0.001 based on a two-tailed Student's t test (and also significant based on a Monte Carlo resampling, as shown by the stippling in Fig. 1, right panel). In contrast, there is no preference for positive or negative Siberian SAT anomalies during the negative phase of the PNA (Figs. 1 and 2a).

To gain insight into why the positive PNA exhibits a strong Siberian positive SAT anomaly and the negative PNA lacks a strong Siberian anomaly of either sign, we calculate composites of the 500-hPa anomalous streamfunction field. This calculation is motivated by Mori and Watanabe (2008) and Franzke et al. (2011), who find that that the positive PNA is preceded by a large amplitude wave train that spans Eurasia and the negative PNA is not. The impact of the Eurasian wave train on the development of the PNA was examined by Dai et al. (2017). They found that the Eurasian wave train propagates southeastward toward the Pacific jet exit region where the wave train anomalies extract kinetic energy from the background flow, as discussed in the introduction, before propagating northeastward toward North America. As can be seen in Fig. 3, even though the streamfunction anomalies tend to somewhat follow a great circle path across the North Pacific and North America, which is consistent with the perspective

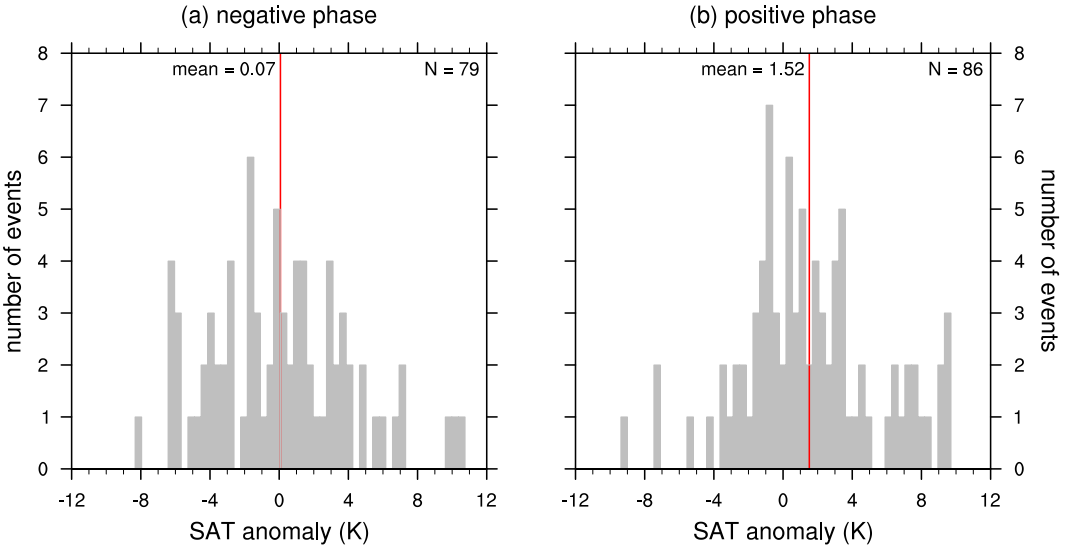

FIG. 2. Histogram showing the number of PNA events (y axis) with a given range of Siberian surface air temperature anomalies at lag day 0 (x axis). (left) The negative PNA phase and (right) the positive PNA phase. The total number of events in each phase is indicated in the top right of each panel and the average Siberian surface air temperature anomaly is indicated by the red vertical line and accompanying text.

that the PNA is driven by tropical convection (Hoskins and Karoly 1981; Horel and Wallace 1981), at negative lags over Eurasia, for both PNA phases, an upstream midlatitude wave train in the streamfunction field is evident (Fig. 3), with this wave train having a substantially larger amplitude for the positive phase of the PNA, consistent with previous findings (Mori and Watanabe 2008; Franzke et al. 2011). A similar wave train can also be seen in the SAT anomaly field, with the amplitude of these anomalies also being much larger for the positive phase (Fig. 1). This result suggests that the Eurasian wave train may influence both the development of the PNA and the presence of the Siberian SAT anomaly only for the positive PNA.

In Fig. 4, we test whether the Eurasian wave train is associated with the Siberian SAT anomaly by dividing positive PNA events based on the histogram shown in Fig. 2b. In particular, we composite the PNA events that lie on the right tail of the distribution shown in Fig. 2b. Those events on the right tail are obtained by iteratively removing the most positive values from the distribution until the mean Siberian SAT anomaly for the remaining distribution is nearly zero. After the right-tail events are removed, the remaining events are used to form the lagged composites in the left column of Fig. 4. The events that were removed from the distribution are used to form the lagged composites in the right column of Fig. 4. With this approach, 18 positive PNA events are identified with an average Siberian SAT anomaly of about 7.36 K at lag day 0. The remaining 68 positive PNA events have an average Siberian SAT anomaly of about −0.03 at lag day 0, which is as close to zero as could possibly be achieved.

We can see in Fig. 4 that both positive PNA composites are characterized by a Rossby wave train propagating over Eurasia at negative lags. However, for those events that are, on average, unassociated with a positive Siberian SAT anomaly, the wave train is muted and displaced southward relative of those events that are associated with the positive Siberian SAT anomaly (cf. right and left columns of Fig. 4). Positive PNA events with a larger amplitude Siberian SAT anomaly are associated with a larger amplitude Eurasian wave train (Fig. 4). Therefore, it is likely that the wave train plays a role in driving the SAT anomaly over Siberia. More evidence for this conclusion is presented in section 3d, which shows that the process driving SAT anomaly growth over Siberia is directly connected to the wave train (Figs. 3 and 4).

b. *Growth and decay*

Having examined the PNA's SAT anomaly pattern, we next shift our focus toward determining what terms in the thermodynamic energy equation drive these SAT anomalies. The leading viewpoint is that SAT anomalies produced on intraseasonal time scales are caused by $-\mathbf{u}' \cdot \nabla\overline{T}$. This viewpoint is rooted in the fact that the SAT anomaly field is usually about 90° out of phase with the sea level pressure anomaly field (e.g., Namias 1978). Such an out-of-phase orientation between the sea level pressure anomaly field and SAT anomaly field can be seen in Fig. 1. This implies a role from $-\mathbf{u}' \cdot \nabla\overline{T}$ on the driving of the SAT anomalies because the SAT anomalies maximize where the zonal sea level pressure gradient maximizes. For example, during the positive PNA, the Aleutian low is enhanced, implying southerly flow over western North America, where the SAT anomaly is positive, and northerly flow over the Russian Far East, where the SAT anomaly is negative (Fig. 1). However, a crucial point is that not all of the SAT anomalies in Fig. 1 are out of phase with the sea level pressure anomalies. For example, over Siberia, during the positive PNA, the SAT anomaly appears without any substantial near-surface circulation anomalies (Fig. 1,

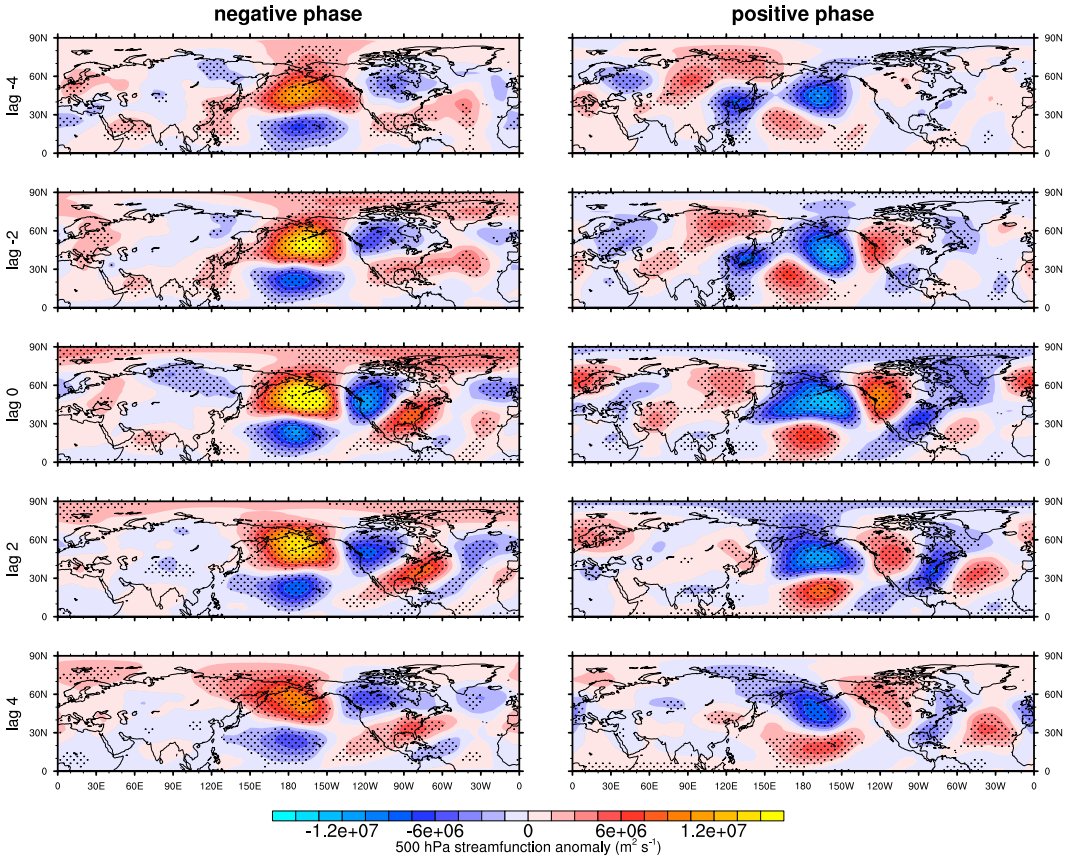

FIG. 3. The 500-hPa streamfunction composite for the (left) negative and (right) positive PNA phases. Rows correspond to different time lags indicated by the left labels in units of days.

contours). Furthermore, for those SAT anomalies that are approximately out of phase with the sea level pressure anomaly field, such an orientation does not preclude the possible contribution to SAT anomalies by other terms in Eq. (1). Thus, further analysis is warranted.

In Fig. 5, we plot composites of the following terms on the lowest η surface, averaged between lag day -2 and lag day $+2$; horizontal advection of the climatological temperature by the anomalous meridional wind, vertical mixing, and longwave radiative heating/cooling. The remaining terms in Eq. (2) are comparatively small (as will be shown in Figs. 6 and 7). As can be seen in Fig. 5, for both PNA phases, the horizontal temperature advection and vertical mixing terms project positively onto the SAT anomaly pattern while the longwave radiative heating rate projects negatively onto the SAT anomaly pattern (cf. Figs. 1 and 5). This implies that both the horizontal temperature advection and vertical mixing terms are important for the growth of the SAT anomaly pattern, while longwave radiative heating/cooling not only opposes the impact of the other two terms, but is likely important for the decay of the SAT anomaly pattern.

Figures 6 and 7 display the SAT anomaly determined from a time integration of each term in Eq. (2). Beginning with the westernmost anomaly of the positive PNA, in Fig. 6a, we show the SAT anomaly averaged over the Siberian box (see Fig. 1). The thick black line shows the composite temperature change over the 21-day integration period while the thin black line shows the integration of the sum of all terms in the thermodynamic energy equation. In this case, the budget is well balanced as the two black lines correspond well. The integrated terms in Eqs. (2) and (3) that contribute to the temperature evolution are given by the various colored lines. Specifically, the red lines correspond to terms in Eq. (3), which includes advection of the climatological temperature by the anomalous wind (thin red), advection of the anomalous temperature by the climatological wind (dashed red) and advection of the anomalous temperature by the anomalous wind (dotted red). The blue lines correspond to diabatic heating terms, including vertical mixing + latent heat release (dashed blue) and longwave radiative heating (thin blue). As can be seen in Fig. 6a, both the growth and the decay of the Siberian SAT anomaly are driven by a single term—vertical mixing, while the remaining terms are comparatively small. This finding is consistent with the fact that the Siberian SAT anomaly is not associated with strong near surface circulation anomalies, based on the sea level pressure anomaly field (Fig. 1). In addition, that both the growth and decay are driven by vertical mixing explains why Fig. 5 shows no vertical mixing anomalies over Siberia. (Figure 5 is a pentad average composite centered on lag day 0.)

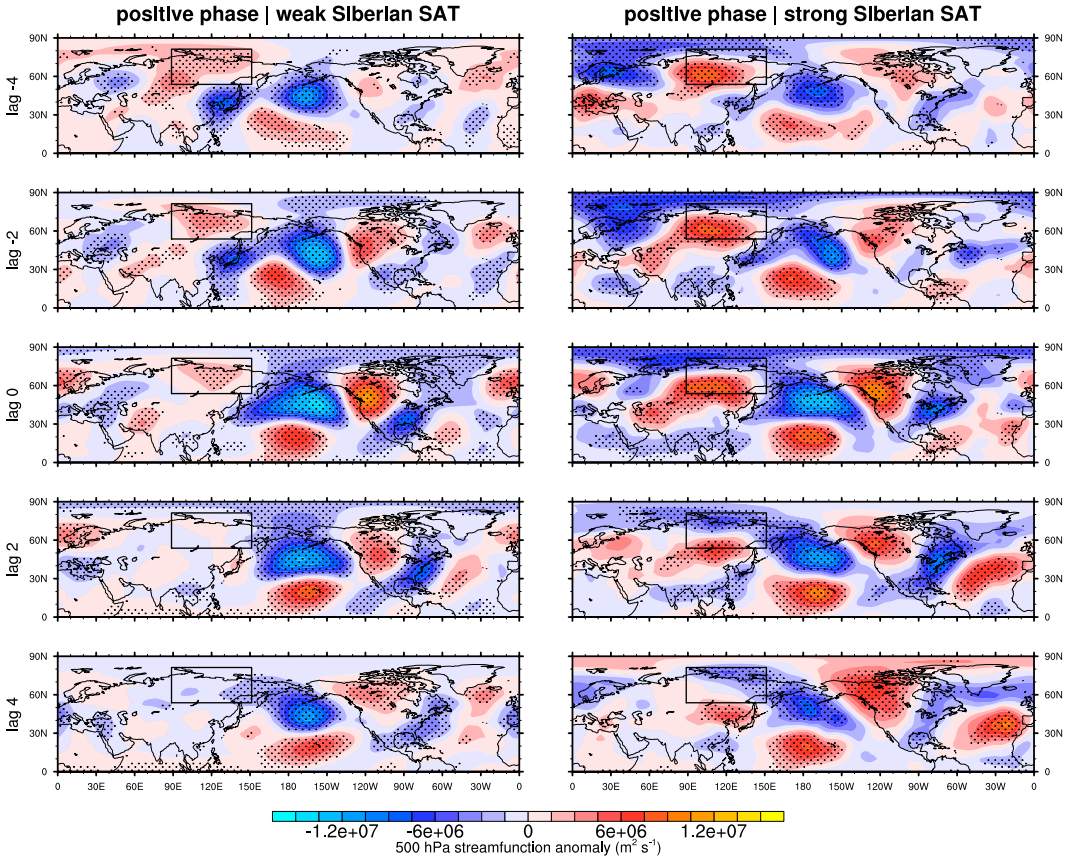

FIG. 4. The 500-hPa streamfunction anomaly composites for the positive PNA phase conditioned on the value of the Siberian surface air temperature anomaly. (left) Positive PNA events that have an average Siberian surface air temperature anomaly of approximately zero. (right) Positive PNA events that have a large positive Siberian surface air temperature anomaly. See text (section 3a) for more details.

Moving east, we continue our analysis of the growth mechanisms for the positive PNA's SAT anomalies. The three SAT anomalies that overlie the Russian Far East and western and eastern North America all lie within a region where there are stronger meridional winds as implied by the sea level pressure gradient, with this gradient being weakest for eastern North America (Fig. 1). Therefore, it is unsurprising that the advection of the climatological temperature by the anomalous wind contributes to the growth for all three of these SAT anomalies (thin red lines, Figs. 6b,c,d). For the negative PNA, three similar SAT anomalies of opposite sign also lie over the Russian Far East and North America. The advection of the climatological temperature by the anomalous wind also contributes to their growth (thin red lines, Figs. 7b,c,d). However, as shown in Fig. 5, all three of these SAT anomalies, for both PNA phases, also have a strong contribution to their growth from vertical mixing (dashed blue lines), with this contribution being largest for eastern North America where the meridional wind anomalies are the smallest. The vertical mixing term is revisited in sections 3c and 3d. The adiabatic and vertical advection contributions to this anomaly are negligible (dotted green and solid green curves), as is the shortwave radiative heating rate, which is not plotted because it does not deviate substantially from zero.

A contrasting feature of the budgets for these three SAT anomalies (that overlie the Russian Far East, western North America, and eastern North America), when compared to that over Siberia, is the fact that the integrated contributions to the SAT anomalies by individual terms in Eqs. (2) and (3) are nearly an order of magnitude greater than the temperature change. This is a consequence of the fact that longwave radiative heating/cooling acts to counter the impact of horizontal temperature advection and vertical mixing. For example, the integrated contribution to the SAT anomaly over the Russian Far East by $-\mathbf{u}' \cdot \nabla\overline{T} + \overline{\mathbf{u}' \cdot \nabla\overline{T}}$, for the negative PNA, is on the order of 12 K while the temperature anomaly, which peaks at lag day 0, attains a maximum value of about 2 K (Fig. 7b). Similar features can be seen for the budgets in the other regions for both PNA phases (Figs. 6 and 7). This implies that without an opposing process (longwave radiative heating/cooling), the temperature anomalies over these regions would attain peak values that are much greater than ~2 K. However, for these three SAT anomalies and for both PNA phases, large integrated values of longwave radiative heating/cooling (thin blue line, Figs. 6 and 7) oppose the growth by horizontal temperature advection and vertical mixing, leading to a near balance. As a result, the summation of

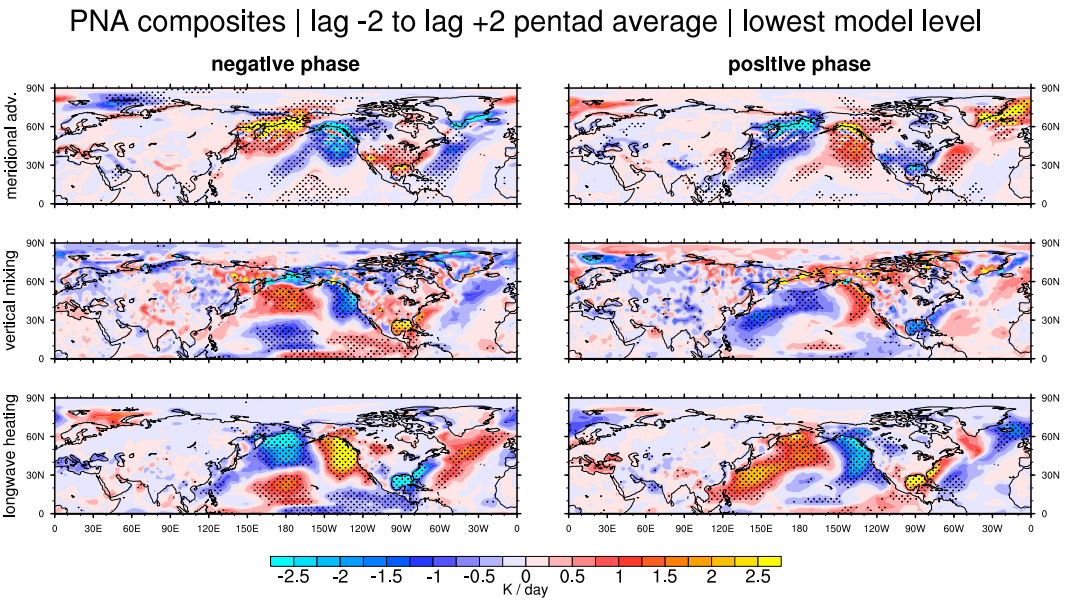

FIG. 5. Composites of (top) $v'\partial\overline{T}/\partial y$, (middle) vertical mixing, and (bottom) longwave radiative heating for the (left) negative and (right) positive PNA phases. The composites are averaged between lag day −2 and lag day +2.

horizontal temperature advection and vertical mixing is slightly stronger than longwave radiative heating/cooling during the growth stage and slightly weaker during the decay stage.

In summary, the growth and decay of each of these SAT anomalies is a consequence of multiple processes acting together. The driving by horizontal temperature advection dominates where the anomalous near surface meridional wind is largest (the Russian Far East and western North America), horizontal temperature advection and vertical mixing make similar contributions where the meridional wind is intermediate (eastern North America), and vertical mixing dominates where the meridional wind is weakest (Siberia and the subtropical North Pacific). The dominant driver of SAT anomaly decay is longwave radiative heating/cooling, except for Siberia. In addition, as will be discussed in section 3d, temperature anomaly decay above the level of the SAT also contributes to SAT anomaly decay, indirectly, by weakening the downgradient diffusion vertical mixing term. The dominant terms during the growth and decay of the PNA are indicated in Table 1.

c. *Conceptualizing longwave radiation and vertical mixing*

We next consider the contribution to SAT anomaly growth by vertical mixing in addition to the contribution to SAT anomaly decay by longwave radiative heating/cooling, with the aim to determine why vertical mixing causes SAT anomaly growth and why longwave radiative heating/cooling causes SAT anomaly decay.

In Fig. 5 (third row), the longwave radiative heating term attains larger amplitudes over the ocean, indicating that longwave radiative heating has a greater damping effect over the ocean than it has over the land. This is because the ocean's temperature, i.e., the sea surface temperature (SST), is relatively constant (due to its large thermal inertia). In the presence of SAT anomalies, the relatively constant SST will result in greater damping by longwave radiation because the upward longwave flux from the ocean *into* the lowest layer will undergo little change while the longwave fluxes *out of* the lowest layer will change greatly. For example, for a positive SAT anomaly, the longwave flux *out of* the lowest layer increases because greater longwave emission occurs at higher temperatures. This leads to a negative longwave radiative heating anomaly because the lowest layer will emit more longwave radiation than it receives from the ocean and vice versa for a negative SAT anomaly. In contrast, over land, where the skin temperature undergoes larger changes than the SST (Clark and Feldstein 2020a), there will be greater anomalous absorption of longwave radiation from below at the lowest layer. This will offset the anomalous emission of longwave radiation at this layer, resulting in reduced damping of the SAT anomaly by longwave radiation over land. It is plausible that this offset over land accounts for the weak longwave cooling over Siberia, allowing for the Siberian SAT anomaly to decay via vertical mixing rather than through longwave radiative cooling.

In Fig. S1 in the online supplemental material, we show a composite of anomalous longwave radiative heating that we computed using the Rapid Radiative Transfer Model for General Circulation Models (RRTMG; Mlawer et al. 1997; Iacono et al. 2008) with the reanalysis surface temperatures (the SSTs and the skin temperatures), air temperatures, water vapor amounts, and surface pressure (Fig. S1, top row) and with surface temperatures set equal to that of the lowest model level (Fig. S1, bottom row). The composite of our RRTMG calculation with the reanalysis surface temperatures corresponds

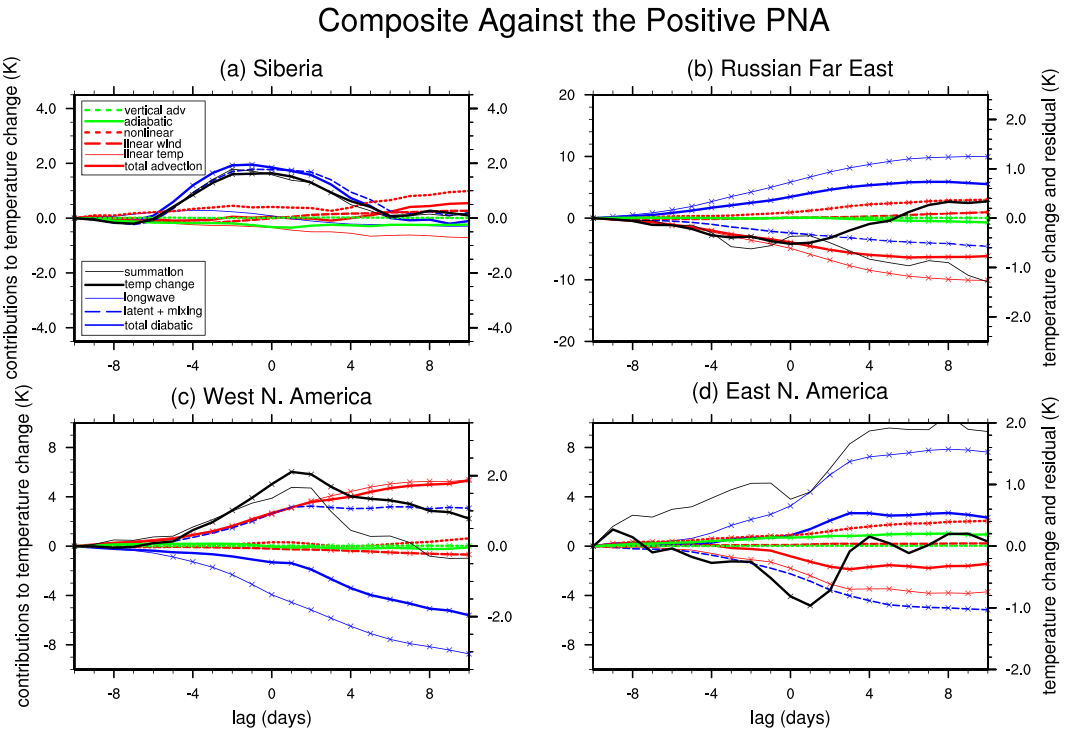

FIG. 6. Composite evolution of temperature anomaly growth and decay on the lowest η surface over (a) Siberia, (b) Russian Far East, (c) western North America, and (d) eastern North America. The thick black line, corresponding to the right y axis, denotes the temperature change averaged over each of the region. The thin black line shows the summed contribution from all of the terms in the thermodynamic energy equation [Eq. (4)]. Those terms include anomalous horizontal temperature advection (i.e., $-\mathbf{u}\cdot\nabla T+\overline{\mathbf{u}\cdot\nabla T}$; thick red line), anomalous diabatic heating (thick blue line), anomalous adiabatic warming (green), and vertical advection (dotted green). The diabatic term (thick blue) is composed of longwave radiative heating (thin blue line) and vertical mixing + latent heat release (dashed blue line). The horizontal advection term in Eq. (3) is composed of $-\mathbf{u}'\cdot\nabla\overline{T}+\overline{\mathbf{u}'\cdot\nabla\overline{T}}$ (linear temperature; thin red line), $-\overline{\mathbf{u}}\cdot\nabla T'+\overline{\overline{\mathbf{u}}\cdot\nabla T'}$ (linear wind; dashed red line), and $-\mathbf{u}'\cdot\nabla T'+\overline{\mathbf{u}'\cdot\nabla T'}$ (nonlinear; dotted red line). All of these terms are integrated using (4), leading to their contribution in units of K.

well with the composite ECMWF longwave heating (cf. Fig. S1, top row, and Fig. 5, bottom row). However, when surface temperatures are set equal to the lowest-model-level temperature, the longwave heating rate at the lowest model level weakens dramatically (Fig. S1, bottom), supporting the mechanism described in the previous paragraph.

Compared to the longwave radiative heating term, the vertical mixing term is more complicated. As stated in section 2b, vertical mixing is a consequence of vertical heat flux convergence (ECMWF 2019). As such, anomalous vertical heat flux convergence drives positive mixing anomalies and anomalous vertical heat flux divergence drives negative mixing anomalies. Furthermore, as discussed in section 2b, vertical heat fluxes arise from a combination of 1) local mixing expressed as downgradient K diffusion and 2) nonlocal mixing that extends throughout much of boundary layer and is characterized by strong updraft mass fluxes.

The nonlocal mixing term is computed by the reanalysis model if the surface layer is unstable, i.e., the surface buoyancy flux is upward (ECMWF 2019). Climatologically, the daily mean winter surface sensible heat flux is upward over much of the extratropics during winter (see Fig. S2). For the PNA's SAT anomaly domains, the climatological daily mean surface sensible heat flux is downward over most of Siberia, upward over all of the subtropical North Pacific, and upward over the water-covered parts of the eastern and western North American and Russian Far East domains, but downward over the land-covered parts of the latter two domains. This implies that nonlocal mixing can have an important impact on the temperature anomalies throughout much of the boundary layer during winter. Also, a downward daily mean surface sensible heat flux does not preclude nonlocal vertical mixing from having an impact on the daily mean vertical mixing because the diurnal cycle of the surface sensible heat flux can be strong over land, as times within the day (especially during the afternoon) may have an upward surface sensible heat flux.

ECMWF determines the downgradient diffusion contribution to vertical mixing using the following expression:

$$\frac{1}{\rho}\frac{\partial F}{\partial z}, \tag{7}$$

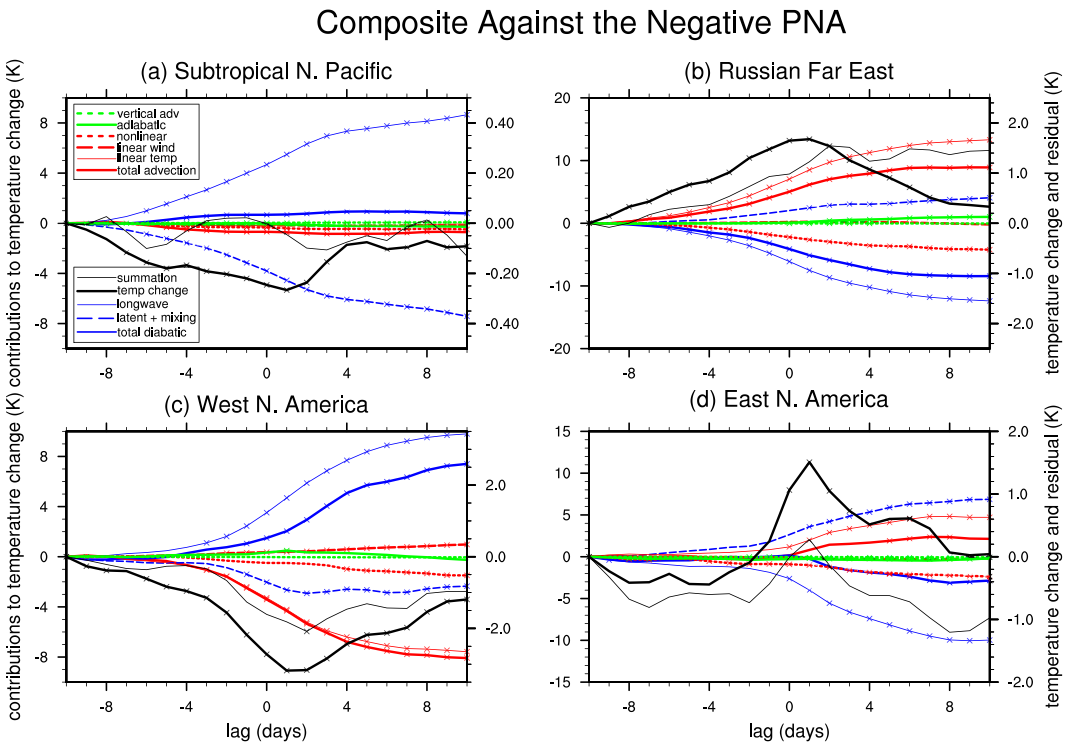

FIG. 7. As in Fig. 6, but for the negative PNA phase and (a) now shows the subtropical North Pacific anomaly, as the negative PNA phase does not typically associate with temperature changes over Siberia (see section 3a).

where $F = \rho K c_p \partial T/\partial z + \rho K g$ is the flux of dry static energy ($c_p T + gz$),[1] ρ is air density, and K is the diffusion coefficient (units: $m^2\ s^{-1}$). In the ECMWF formulation, K varies in latitude, longitude, height, and time. ECMWF provides K as a downloadable variable, enabling us to compute composites of anomalies in F for both the positive and negative PNA phases (Fig. S3).

As can be seen in Fig. S3, for some positive SAT anomalies, the diffusive heat fluxes are downward throughout the boundary layer. This is true for both land and some oceanic parts of the western North American (positive PNA) and eastern North American (negative PNA) domains where the boundary layer height is 450–600 m (not shown) and for the Siberian domain (positive PNA) where the boundary layer height is only about 150 m (not shown). For all the other SAT anomalies, where the boundary layer is much deeper, the downgradient diffusive heat fluxes are downward in the lower half of the boundary layer, and upward in the upper half of the boundary layer. This indicates that downgradient diffusion is relocating temperature anomalies from higher in the boundary layer downward toward the surface, suggesting that diffusive mixing contributes to temperature anomaly growth in the lower half of the boundary layer.

[1] In addition to dry static energy, ERA-Interim does include specific liquid water and specific ice water in this flux. However, the flux of these two quantities is expected to be very small in the lower part of the boundary layer.

In Figs. S4 and S5, we show that vertical mixing damps the temperature anomalies throughout the boundary layer, except at the lowest two levels, where vertical mixing contributes to temperature anomaly growth. We expect the nonlocal vertical mixing contribution (turbulence associated with convection) to damp the PNA's temperature anomalies *at all levels* in the boundary layer for the following reasons:

1) Anomalies of $d\theta/dz$ are negative throughout the boundary layer for negative SAT anomalies and vice versa for positive SAT anomalies over the North Pacific and western and eastern North America (not shown).
2) With the exception of Siberia, an examination of the anomalous surface sensible heat flux in each domain for both PNA phases (Fig. S3, top panels) indicates that the anomalous surface sensible heat flux is upward where the SAT anomaly is negative and vice versa. This indicates that the boundary layer is more unstable (stable) relative to the climatology above negative (positive) SAT anomalies and therefore suggests that nonlocal mixing being should be anomalously strong (weak) above negative (positive) SAT anomalies.
3) The anomalous updraft mass fluxes are upward for the negative SAT anomalies and downward for positive SAT anomalies over the North Pacific and western and eastern North America (Fig. 11), as will be discussed more in section 3d, where we present more evidence that the nonlocal mixing term is active over each SAT domain. All three factors listed above promote an anomalous upward

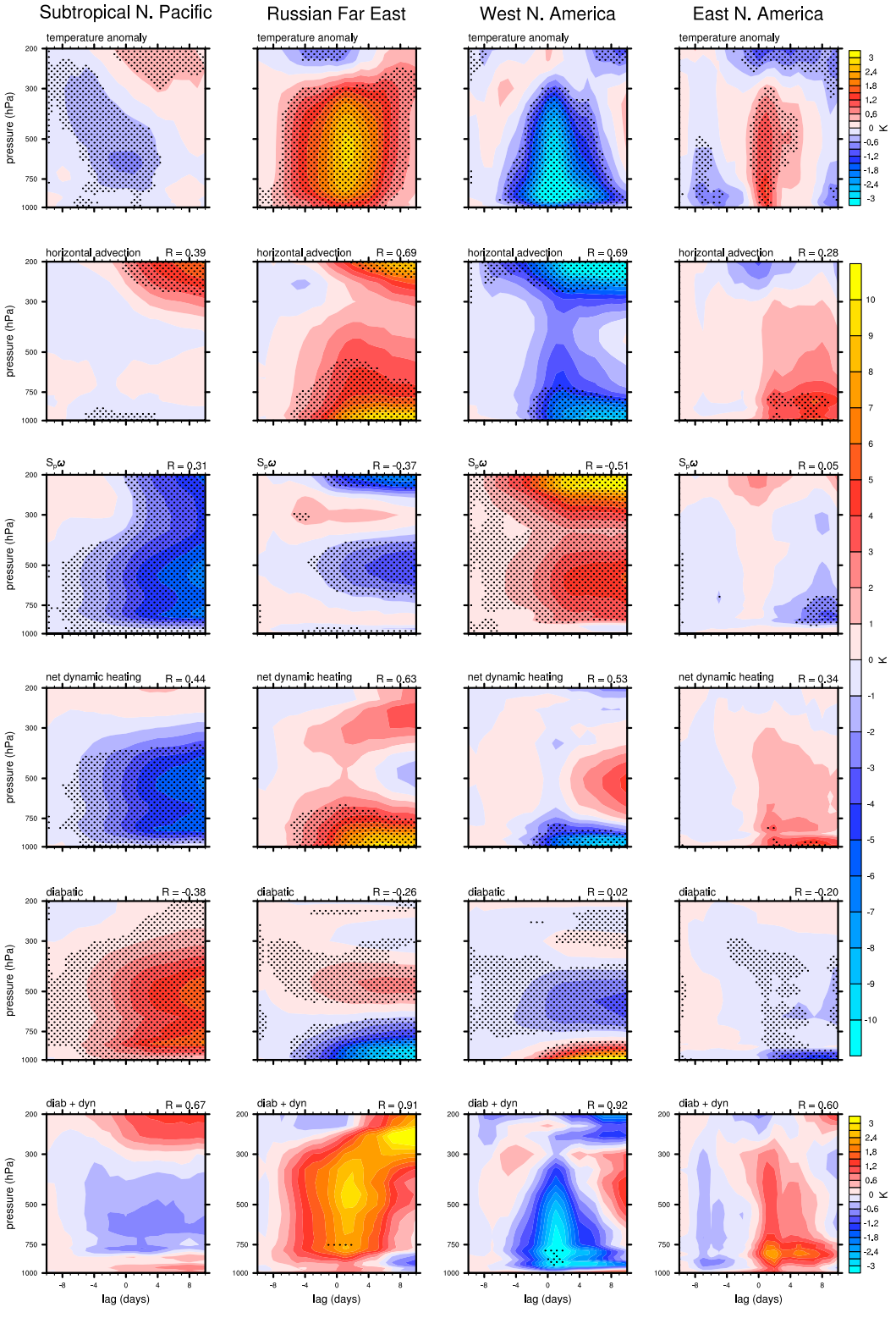

FIG. 8. Composite evolution of temperature anomaly growth and decay as a function of pressure (y axis) and lag day (x axis) for the negative PNA. The (row 1) composite temperature anomaly change, (row 2) integrated anomalous horizontal temperature advection, (row 3) integrated $S_p\omega$, (row 4) row 2 + row 3, (row 5) diabatic heating, and (row 6) row 4 + row 5 are shown. The columns correspond to the region indicated. Each term is area averaged over the indicated region and integrated using (4) (see section 2b).

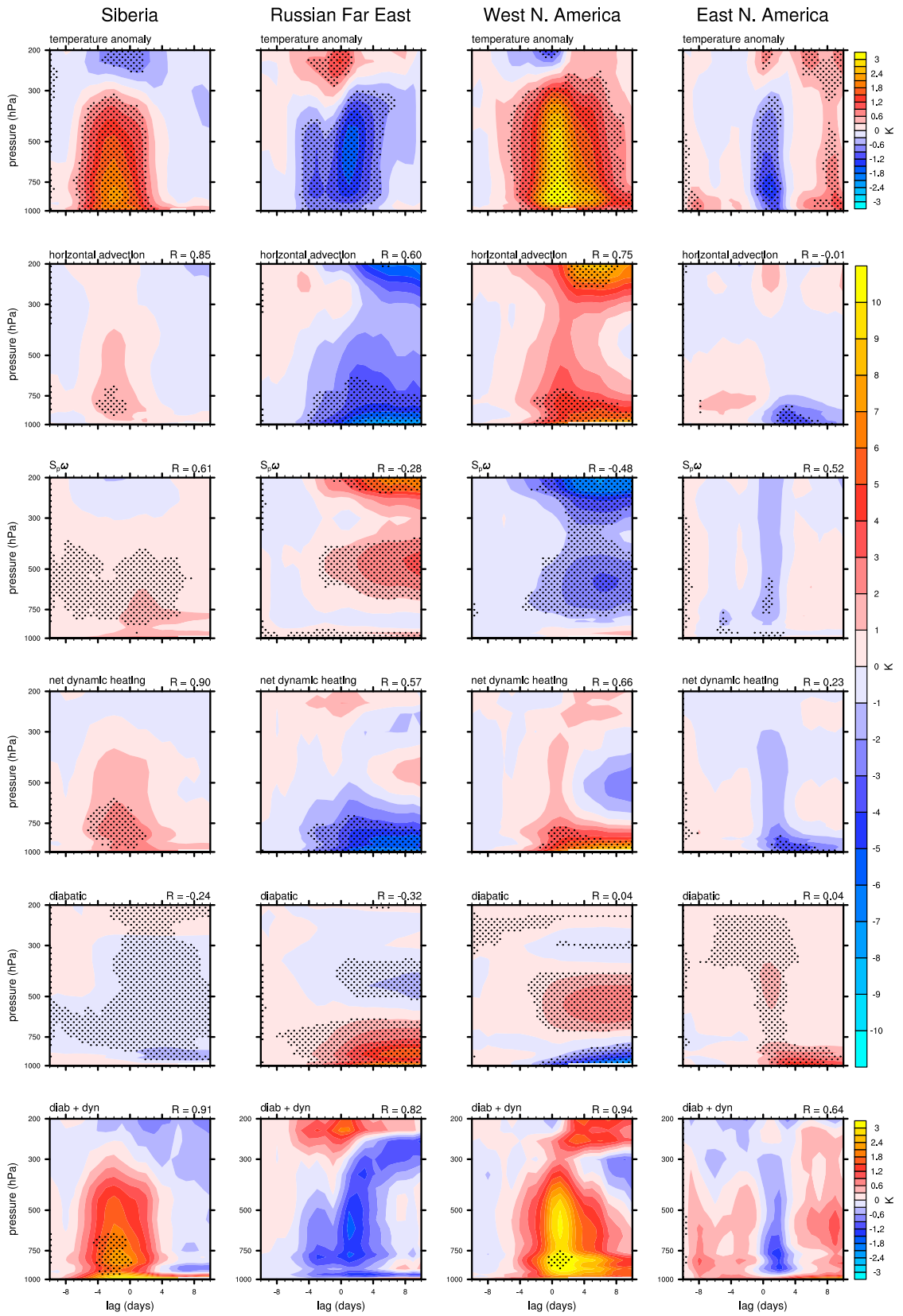

FIG. 9. As in Fig. 8, but for the positive PNA.

convective heat transport for negative SAT anomalies, resulting in a warming of the boundary layer, and vice versa for positive SAT anomalies. Because vertical mixing enhances the temperature anomalies on the two lowest model levels, we therefore conclude that the vertical mixing anomalies on the lowest two model levels are a consequence of local downgradient diffusive mixing.

d. *The vertical temperature profile*

In section 3b, we showed that both horizontal temperature advection and vertical mixing are the dominant contributors driving the temperature anomalies at the lowest model level, with some anomalies being dominated by the former, some by the latter, and others by both. In section 3c, we showed that vertical mixing at the lowest model level is largely caused by downward diffusive heat fluxes from levels higher in the boundary layer (Fig. S3). Therefore, at the lowest model level, in addition to driving by horizontal temperature advection, processes that take place above the lowest model level are also behind much of the driving of the lowest-model-level temperature anomalies. This applies to both the growth and decay stages of the lowest-model-level anomalies: As the temperature anomalies above the lowest model level strengthen, due to horizontal temperature advection (Figs. S6 and S7), in response, mixing from local downgradient diffusion strengthens the temperature anomalies at the lowest model level. However, nonlocal mixing also weakens the temperature anomalies throughout the boundary layer (Figs. S4 and S5). Therefore, decay of the SAT anomalies can be thought of as resulting from a combination of damping by longwave radiative heating/cooling and an indirect weakening of downgradient diffusion that arises from nonlocal mixing higher in the boundary layer.

In light of this, in the remaining figures (Figs. 8–11), we investigate what processes lead to temperature anomaly growth and decay throughout the troposphere, as these processes ultimately are contributing to vertical mixing anomalies at the surface. Our conclusion is that dynamical processes drive temperature anomalies throughout the troposphere, and diffusive vertical mixing communicates their effect to the surface.

To show this, we begin with Figs. 8 and 9, for the negative and positive PNA phases, respectively, by illustrating the vertical temperature profile of the temperature anomalies obtained by integrating various terms in the thermodynamic energy equation, as discussed in section 2. Although these figures contain a multitude of panels, the essence of the results can be summed up in a few sentences. Dynamical processes drive temperature anomaly growth (primarily horizontal temperature advection, but in the case of eastern North America and the subtropical North Pacific, also adiabatic warming/cooling). Diabatic processes drive temperature anomaly decay. These conclusions can be drawn by comparing the topmost rows of Figs. 8 and 9 to the subsequent rows, where it is seen that the rows corresponding to horizontal temperature advection and adiabatic warming/cooling (rows 2 through 4) are the only panels that have the same sign as the temperature

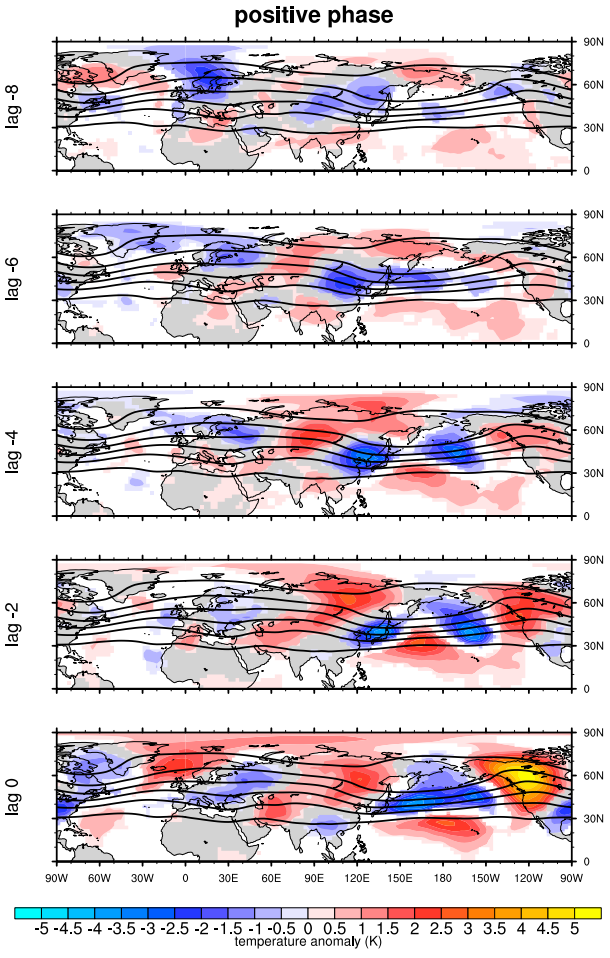

FIG. 10. Composite 500-hPa temperature anomaly (shading) for the positive PNA. The climatological 500-hPa geopotential height is shown in black contours. The geopotential height contour interval is 100 m, with values ranging from 5300 to 5800 m shown.

anomaly. The diabatic heating term (row 5) is generally opposite in sign with the temperature anomaly, indicating a contribution to temperature anomaly decay.

In the supplementary section we provide further analysis (Figs. S8 and S9) to determine the main contributor to the horizontal temperature advection. We find that $-\mathbf{u}' \cdot \nabla\overline{T} + \overline{\mathbf{u}' \cdot \nabla\overline{T}}$ is the dominant contributor to horizontal temperature advection, with the exception being Siberia, where $-\overline{\mathbf{u}} \cdot \nabla T' + \overline{\mathbf{u}} \cdot \nabla T'$ is largest (Figs. S8 and S9). For $-\mathbf{u}' \cdot \nabla\overline{T} + \overline{\mathbf{u}' \cdot \nabla\overline{T}}$, which corresponds to the advection of the climatological temperature field by the anomalous wind, it is the circulation anomalies of the PNA (Fig. 3) that are driving the temperature anomalies. This is followed by mixing, via downgradient diffusion, which relocates the temperature anomalies down to the level of the SAT.

The result that $-\overline{\mathbf{u}} \cdot \nabla T' + \overline{\mathbf{u}} \cdot \nabla T'$ is dominant over Siberia for the positive phase is further evidence that the SAT asymmetry over Siberia (Fig. 1) is indeed a consequence of the Eurasian wave train (Figs. 3 and 4). Inspection of Fig. 3

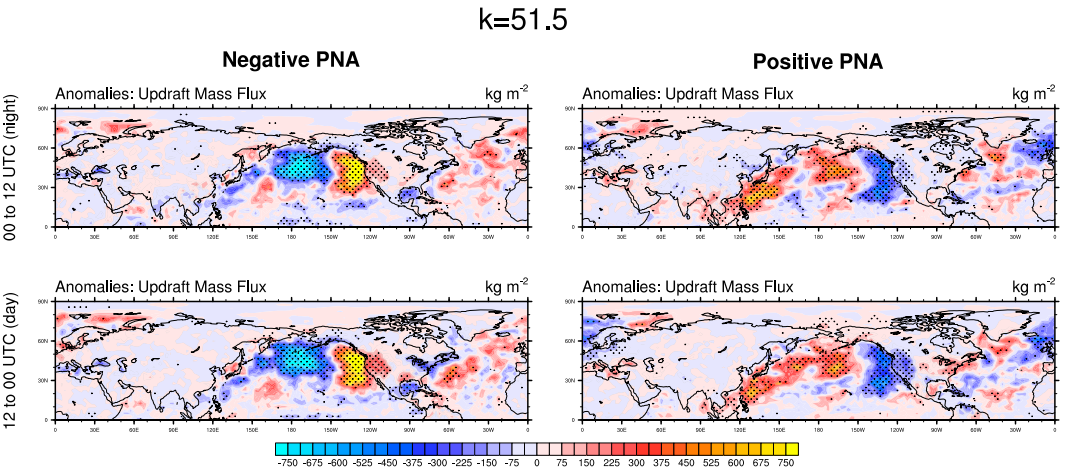

FIG. 11. Anomalous updraft mass flux at the $k = 51.5$ half model level averaged (top) from 0000 to 1200 UTC and (bottom) from 1200 to 0000 UTC.

suggests that the temperature anomalies in the wave train are triggered by $-\mathbf{u}' \cdot \nabla\overline{T} + \mathbf{u}' \cdot \nabla\overline{T}$ upstream of Siberia. The wave train then propagates downstream as the climatological wind $\overline{\mathbf{u}}$ advects both streamfunction and temperature anomalies (Fig. 10). The temperature anomalies eventually become positioned over Siberia where diffusive vertical mixing communicates the temperature anomalies to the lowest η surface. This chain of events can be seen in Fig. 10. These features contrast the negative PNA events, and the positive PNA events without a large Siberian SAT anomaly, as the upstream Eurasian wave train has a small amplitude which does not trigger temperature anomalies to be advected downstream by the climatological jet, resulting in the absence of temperature anomalies to be diffused downward to the surface.

The diabatic heating term (row 5 of Figs. 8 and 9) is decomposed into its contributions in Figs. S10 and S11. Interestingly, the dominant diabatic heating term contributing to temperature anomaly decay in the boundary layer and lower troposphere is most often vertical mixing (Figs. S10 and S11), indicating a reversal of its role at the two lowest levels, as discussed in section 3c. Furthermore, as was discussed in section 3c, the reason for vertical mixing changing sign in the boundary layer is primarily a consequence of nonlocal vertical mixing. Figure 11, which shows anomalous updraft mass fluxes, provides further evidence for the role of nonlocal vertical mixing.

The composite anomalous updraft mass fluxes for the PNA averaged between 0000 and 1200 UTC and 1200 and 0000 UTC at the $k = 51.5$ model level, which corresponds to approximately the 925-hPa level, are shown in Fig. 11 (Berrisford et al. 2009; these quantities are 12-h accumulations downloaded from ERA-Interim). As can be seen, the anomalous updraft mass fluxes tend to be positive where there are negative SAT anomalies and vice versa, providing further support for the perspective discussed in the preceding section that nonlocal mixing via cumulus updrafts has a large influence on the temperature field in the boundary layer above the two lowest model levels. Furthermore, over land, the daytime updraft anomalous mass fluxes are stronger than the nighttime anomalous updraft mass fluxes, revealing, as expected, that nonlocal mixing has its largest impact during the daytime. In terms of total fields, updraft mass fluxes are strongly positive throughout all of the water-covered parts of each domain (Fig. S12), and even over some of the land parts of the western and eastern North American domains, indicating the presence of nonlocal boundary layer–scale mixing and convection (ECMWF 2019). Over Siberia, there is very little updraft mass flux, as expected from the climatological surface sensible heat flux (Fig. S2). This suggests that downgradient diffusion may be dominating the mixing throughout the boundary layer over Siberia.

Except for Siberia and the subtropical North Pacific, horizontal temperature advection may have played a role in driving updrafts and nonlocal vertical mixing. This is because vertical mixing is anomalously positive in Figs. S4 and S5 (except for the two lowest model levels) over locations where the stability of the atmosphere has been decreased by horizontal temperature advection, and vice versa (Figs. S6 and S7; these temperatures resemble the actual temperatures in the boundary layer). As can be seen, the temperature anomalies due to horizontal temperature advection decrease with increasing height at locations where the anomalous updraft and mixing terms are positive (Figs. S4, S5, S6, and S7 and Fig. 11). Contrastingly, regions where vertical mixing is anomalously negative in Figs. S4 and S5 are regions where the stability of the atmosphere has been increased by horizontal temperature advection (the temperature due to horizontal temperature advection increases with height; Figs. S6 and S7). This finding suggests that horizontal temperature advection plays an important role in determining the strength of nonlocal vertical mixing in the boundary layer.

4. Summary and conclusions

We have examined the temperature anomaly pattern associated with the PNA teleconnection, showing that there are both symmetric and asymmetric SAT anomalies for the two

PNA phases. The symmetric SAT anomalies, which are found in both PNA phases, are located over the Russian Far East, western and eastern North America, and grow by both horizontal temperature advection and vertical mixing. In contrast, the asymmetric SAT anomalies are limited to one phase, being found over Siberia in the positive phase and over the subtropical North Pacific in the negative PNA phase. The asymmetric SAT anomaly over Siberia is linked to a wave train that propagates over Eurasia preferentially during the positive PNA phase. The two asymmetric SAT anomalies over Siberia and the subtropical North Pacific grow via vertical mixing. All of the SAT anomalies, except for the subtropical North Pacific SAT anomaly, are driven either directly by horizontal temperature advection at the level of the SAT, as indicated above, or indirectly by horizontal temperature advection higher in the atmosphere, after which these temperature anomalies are relocated downward to the level of the SAT via vertical mixing. The subtropical North Pacific SAT anomaly is driven indirectly by adiabatic cooling in the free atmosphere, whose impact is relocated to the level of the SAT via vertical mixing. The decay of all SAT anomalies is through longwave radiative heating/cooling, except for Siberia which decays via vertical mixing.

Altogether, these results highlight a diversity of processes that contribute to SAT anomaly growth and decay when the PNA is active. For those SAT anomalies which are driven by horizontal temperature advection, the near surface anomalous winds are relatively strong. In contrast, the SAT anomalies driven by vertical mixing are characterized by very weak anomalous winds near the surface. Since horizontal temperature advection at the level of the SAT is driven primarily by the advection of the climatological temperature by the anomalous wind, it is not surprising that horizontal temperature advection weakly contributes to SAT anomalies where vertical mixing is dominant.

As indicated above, the decay of all the SAT anomalies, except for that over Siberia, is through anomalous longwave radiative heating/cooling. The Siberian SAT anomaly differs from all the other SAT anomalies as it is almost entirely over land. It is found that the anomalous longwave radiative heating/cooling is much stronger over water than over land. Over water, at the level of the SAT, the anomalous emission of longwave radiation must dominate the absorption, since the SST undergoes little change. This contrasts land areas, where the anomalous skin temperature is closer to the anomalous SAT, resulting in the anomalous emission and absorption being similar.

Our analysis of the vertical mixing term reveals that local downgradient diffusive mixing amplifies the temperature anomalies at the two lowest model levels. In contrast, throughout the rest of the boundary layer, nonlocal mixing via convective updrafts damps the temperature anomalies. Since these parameterized processes play a large role in the growth and decay of the SAT anomalies associated with the PNA pattern, these results emphasize the importance of correctly parameterizing vertical mixing, as this term can lead to changes in the evolution of the PNA.

Acknowledgments. We thank three anonymous reviewers for their helpful comments and questions. This study benefitted from research discussions with Sukyoung Lee, Ying Pan, David Stensrud, Cory Baggett, Mingyu Park, Dong Wan Kim, Colton Milcarek, and Allen Mewhinney. This study was supported by National Science Foundation Grants OPP-1723832 and AGS-1822015.

Data availability statement. The data used in this study can be downloaded from the ECMWF archive (https://apps.ecmwf.int/datasets/data/interim-full-daily/levtype=sfc/). The PNA index used in this study can be downloaded from the NOAA/Climate Prediction Center website (https://www.cpc.ncep.noaa.gov/products/precip/CWlink/pna/pna.shtml).

REFERENCES

Barnston, A. G., and R. E. Livezey, 1987: Classification, seasonality and persistence of low-frequency atmospheric circulation patterns. *Mon. Wea. Rev.*, **115**, 1083–1126, https://doi.org/10.1175/1520-0493(1987)115<1083:CSAPOL>2.0.CO;2.

Berrisford, P., D. Dee, K. Fielding, M. Fuentes, P. Kallberg, S. Kobayashi, and S. Uppala, 2009: The ERA Interim Archive: Version 1.0. ECMWF ERA Rep. Series, 16 pp., http://ecmwf.int/publications/library/do/references/show?id=89203.

Black, R. X., and R. M. Dole, 1993: The dynamics of large-scale cyclogenesis over the North Pacific. *J. Atmos. Sci.*, **50**, 421–442, https://doi.org/10.1175/1520-0469(1993)050<0421:TDOLSC>2.0.CO;2.

Blackmon, M. L., Y. H. Lee, and J. M. Wallace, 1984a: Horizontal structure of 500 mb height fluctuations with long, intermediate and short time scales. *J. Atmos. Sci.*, **41**, 961–980, https://doi.org/10.1175/1520-0469(1984)041<0961:HSOMHF>2.0.CO;2.

——, ——, ——, and H. H. Hsu, 1984b: Time variation of 500 mb height fluctuations with long, intermediate and short time scales as deduced from lag-correlation statistics. *J. Atmos. Sci.*, **41**, 981–991, https://doi.org/10.1175/1520-0469(1984)041<0981:TVOMHF>2.0.CO;2.

Branstator, G., 1990: Low-frequency patterns induced by stationary waves. *J. Atmos. Sci.*, **47**, 629–649, https://doi.org/10.1175/1520-0469(1990)047<0629:LFPIBS>2.0.CO;2.

——, 1992: The maintenance of low-frequency atmospheric anomalies. *J. Atmos. Sci.*, **49**, 1924–1946, https://doi.org/10.1175/1520-0469(1992)049<1924:TMOLFA>2.0.CO;2.

Cash, B. A., and S. Lee, 2001: Observed nonmodal growth of the Pacific–North American teleconnection pattern. *J. Climate*, **14**, 1017–1028, https://doi.org/10.1175/1520-0442(2001)014<1017:ONGOTP>2.0.CO;2.

Clark, J. P., and S. B. Feldstein, 2020a: What drives the North Atlantic Oscillation's temperature anomaly pattern? Part I: The growth and decay of the surface air temperature anomalies. *J. Atmos. Sci.*, **77**, 185–198, https://doi.org/10.1175/JAS-D-19-0027.1.

——, and ——, 2020b: What drives the North Atlantic Oscillation's temperature anomaly pattern? Part II: A decomposition of the surface downward longwave radiation anomalies. *J. Atmos. Sci.*, **77**, 199–216, https://doi.org/10.1175/JAS-D-19-0028.1.

——, V. Shenoy, S. B. Feldstein, S. Lee, and M. Goss, 2021: The role of horizontal temperature advection on Arctic

amplification. *J. Climate*, **34**, 2957–2976, https://doi.org/10.1175/JCLI-D-19-0937.1.

Dai, Y., S. B. Feldstein, B. Tan, and S. Lee, 2017: Formation mechanisms of the Pacific–North American teleconnection with and without its canonical tropical convection pattern. *J. Climate*, **30**, 3139–3155, https://doi.org/10.1175/JCLI-D-16-0411.1.

Dee, D. P., and Coauthors, 2011: The ERA-Interim reanalysis: Configuration and performance of the data assimilation system. *Quart. J. Roy. Meteor. Soc.*, **137**, 553–597, https://doi.org/10.1002/qj.828.

Dickson, R. R., and J. Namias, 1976: North American influences on the circulation and climate of the North Atlantic sector. *Mon. Wea. Rev.*, **104**, 1255–1265, https://doi.org/10.1175/1520-0493(1976)104<1255:NAIOTC>2.0.CO;2.

ECMWF, 2014: IFS documentation Cy40r1—Part III: Dynamics and numerical procedures. ECMWF Doc., 31 pp., https://doi.org/10.21957/juw9gfhn2.

——, 2019: IFS documentation CY46r1—Part IV: Physical processes. ECMWF Doc., 223 pp., https://doi.org/10.21957/xphfxep8c.

Feldstein, S. B., 2000: The timescale, power spectra, and climate noise properties of teleconnection patterns. *J. Climate*, **13**, 4430–4440, https://doi.org/10.1175/1520-0442(2000)013<4430:TTPSAC>2.0.CO;2.

——, 2002: Fundamental mechanisms of the growth and decay of the PNA teleconnection pattern. *Quart. J. Roy. Meteor. Soc.*, **128**, 775–796, https://doi.org/10.1256/0035900021643683.

Franzke, C., S. B. Feldstein, and S. Lee, 2011: Synoptic analysis of the Pacific–North American teleconnection pattern. *Quart. J. Roy. Meteor. Soc.*, **137**, 329–346, https://doi.org/10.1002/qj.768.

Harding, K. J., and P. K. Snyder, 2015: The relationship between the Pacific–North American teleconnection pattern, the Great Plains low-level jet, and north central U.S. heavy rainfall events. *J. Climate*, **28**, 6729–6742, https://doi.org/10.1175/JCLI-D-14-00657.1.

Holton, J. R., and G. H. Hakim, 2013: *An Introduction to Dynamic Meteorology*. 5th ed. Academic Press, 532 pp.

Horel, J. D., and J. M. Wallace, 1981: Planetary-scale atmospheric phenomena associated with the Southern Oscillation. *Mon. Wea. Rev.*, **109**, 813–829, https://doi.org/10.1175/1520-0493(1981)109<0813:PSAPAW>2.0.CO;2.

Hoskins, B. J., and D. J. Karoly, 1981: The steady linear response of a spherical atmosphere to thermal and orographic forcing. *J. Atmos. Sci.*, **38**, 1179–1196, https://doi.org/10.1175/1520-0469(1981)038<1179:TSLROA>2.0.CO;2.

Iacono, M. J., J. S. Delamere, E. J. Mlawer, M. W. Shephard, S. A. Clough, and W. D. Collins, 2008: Radiative forcing by long-lived greenhouse gases: Calculations with the AER radiative transfer models. *J. Geophys. Res.*, **113**, D13103, https://doi.org/10.1029/2008JD009944.

Leathers, D. J., B. Yarnal, and M. A. Palecki, 1991: The Pacific/North American teleconnection pattern and United States climate. Part I: Regional temperature and precipitation associations. *J. Climate*, **4**, 517–528, https://doi.org/10.1175/1520-0442(1991)004<0517:TPATPA>2.0.CO;2.

Leith, C. E., 1973: The standard error of time-average estimates of climatic means. *J. Appl. Meteor.*, **12**, 1066–1069, https://doi.org/10.1175/1520-0450(1973)012<1066:TSEOTA>2.0.CO;2.

Madden, R. A., 1976: Estimates of the natural variability of time-averaged sea-level pressure. *Mon. Wea. Rev.*, **104**, 942–952, https://doi.org/10.1175/1520-0493(1976)104<0942:EOTNVO>2.0.CO;2.

——, and D. J. Shea, 1978: Estimates of the natural variability of time-averaged temperatures over the United States. *Mon. Wea. Rev.*, **106**, 1695–1703, https://doi.org/10.1175/1520-0493(1978)106<1695:EOTNVO>2.0.CO;2.

Mlawer, E. J., S. J. Taubman, P. D. Brown, M. J. Iacono, and S. A. Clough, 1997: Radiative transfer for inhomogeneous atmospheres: RRTM, a validated correlated-k model for the longwave. *J. Geophys. Res.*, **102**, 16 663–16 682, https://doi.org/10.1029/97JD00237.

Mori, M., and M. Watanabe, 2008: The growth and triggering mechanisms of the PNA: A MJO-PNA coherence. *J. Meteor. Soc. Japan*, **86**, 213–236, https://doi.org/10.2151/jmsj.86.213.

Namias, J., 1969: Seasonal interactions between the North Pacific Ocean and the atmosphere during the 1960's. *Mon. Wea. Rev.*, **97**, 173–192, https://doi.org/10.1175/1520-0493(1969)097<0173:SIBTNP>2.3.CO;2.

——, 1978: Multiple causes of the North American abnormal winter 1976–77. *Mon. Wea. Rev.*, **106**, 279–295, https://doi.org/10.1175/1520-0493(1978)106<0279:MCOTNA>2.0.CO;2.

Notaro, M., W. C. Wang, and W. Gong, 2006: Model and observational analysis of the northeast U.S. regional climate and its relationship to the PNA and NAO patterns during early winter. *Mon. Wea. Rev.*, **134**, 3479–3505, https://doi.org/10.1175/MWR3234.1.

Seo, K. H., H. J. Lee, and D. M. Frierson, 2016: Unraveling the teleconnection mechanisms that induce wintertime temperature anomalies over the Northern Hemisphere continents in response to the MJO. *J. Atmos. Sci.*, **73**, 3557–3571, https://doi.org/10.1175/JAS-D-16-0036.1.

Simmons, A. J., J. Wallace, and G. W. Branstator, 1983: Barotropic wave propagation and instability, and atmospheric teleconnection patterns. *J. Atmos. Sci.*, **40**, 1363–1392, https://doi.org/10.1175/1520-0469(1983)040<1363:BWPAIA>2.0.CO;2.

Walker, G. T., and E. W. Bliss, 1932: World weather V. *Mem. J. Roy. Meteor. Soc.*, **4**, 53–84.

Wallace, J. M., and D. S. Gutzler, 1981: Teleconnections in the geopotential height field during the Northern Hemisphere winter. *Mon. Wea. Rev.*, **109**, 784–812, https://doi.org/10.1175/1520-0493(1981)109<0784:TITGHF>2.0.CO;2.

Yu, B., and H. Lin, 2019: Modification of the wintertime Pacific–North American pattern related North American climate anomalies by the Asian–Bering–North American teleconnection. *Climate Dyn.*, **53**, 313–328, https://doi.org/10.1007/s00382-018-4586-4.